INTERPLAY BETWEEN SHAPE AND COMPOSITION IN THE COMPRESSIVE RESPONSE OF ALUMINUM FOAMS

JAROSLAV KOVÁČIK[1], JAROSLAV JERZ[1], FRANTIŠEK SIMANČÍK[1], ANDREJ OPÁLEK[1], SELIM BURAK CANTÜRK[1,2], LIVIU MARSAVINA[3,4], EMANOIL LINUL[4]

Abstract. Comprehending the interplay between foam morphology, surface skin, geometry, and compressive behavior is fundamental to the design of advanced functional applications, including energy absorption (EA) systems, seismic mitigation devices, and Phase Change Material heat storage units. The influence of sample shape (cylinder-CYL, triangular prism-TRP and square prism-SQP) on microstructural and compression behavior was investigated for ductile (AlMg1Si0.6 + 1% wt. ZrH_2) and brittle (AlSi12Mg0.6 + 0.4% wt. TiH_2) aluminum alloy foams (AAFs). The different compositions and foaming agents led to unique cellular structures. The AAF structures exhibited heterogeneity, with variations between top and bottom parts of samples, but only small differences in pore numbers were observed. Total number of pores varied according to the cross-sectional shape, with CYLs having significantly more pores compared to TRPs and SQPs. Ductile AAF had small round pores with thick pore walls, while brittle AAFs exhibited regions with dense and thin pore structures due to coalescence and collapse during foaming. Precursor composition significantly impacted AAF structure, surface skin thickness, and compression. Compression strength, plateau stress, and EA were shape-dependent: SQPs performed best for brittle AAFs, while CYL samples showed higher ductile compression response and better EA in brittle AAFs. Densification strain was again observed independent on the sample shape, type of alloy, type and amount of foaming agent.

Key words: aluminum foams, shape effect, alloy composition, compressive behavior, microstructure, mechanical properties.

1. INTRODUCTION

Aluminum alloy foam (AAF) [1–4] columns could have various shapes and sizes, depending on their intended use. Usually for large scale application of foams

[1] Institute of Materials and Machine Mechanics SAS, Dúbravská cesta 9/6319, 845 13 Bratislava, Slovakia
[2] Faculty of Mechanical Engineering, Slovak University of Technology, Námestie slobody 17, 812 31 Bratislava, Slovakia
[3] Romanian Academy – Timisoara Branch, Blvd. M. Viteazu, No. 24, Timisoara 300223, Romania
[4] Department of Mechanics and Strength of Materials, "Politehnica" of University Timisoara, 1 Mihai Viteazu Avenue, 300 222, Timisoara, Romania

Ro. J. Techn. Sci. − Appl. Mechanics, Vol. 70, N^{os} 1–3, P. 113–129, Bucharest, 2025

DOI:10.59277/RJTS-AM.2025.1-3.07

in energy absorber [5–7], earthquake resistant structures [8], and large latent heat batteries [9–10] it is necessary to create large foam blocks using large number of smaller pieces of foam. Such structures could be combined from cylindrical, square, rectangular, hexagonal or triangle shapes or their combinations.

During the century of the AAF preparation [11–15] and half a century old history of measurement of their mechanical and physical properties [16–37], the compression tests are mostly performed on cylindrical or prismatic/cubic specimens [38–46]. Moreover, the presence of surface skin, especially for powder metallurgical (PM) metallic foams, significantly influences the compression results.

Nevertheless, additional experimental investigations are required to verify whether the reported findings can be generalized to other AAFs. Variations in the amount of foaming agent used can result in significantly different foam structures [47]; therefore, it remains to be determined how these structural differences influence the outcomes of compression tests for various sample geometries. Therefore, the objective of this study is to further examine the influence of sample geometry on the quasi-static compression behavior of ductile, closed-cell AAFs (AlMg1Si0.6) with a surface skin, produced using 1 wt.% zirconium hydride as a foaming agent, as well as of brittle AAFs (AlSi12Mg0.6) containing a smaller amount of foaming agent (0.4 wt.% TiH_2).

2. MATERIALS AND METHODS

AAF samples were prepared by PM process from the two different aluminum alloys precursors: ductile AlMg1Si0.6 + 1% wt. ZrH_2 and brittle AlSi12Mg0.6 + 0.4% wt. TiH_2. The samples were foamed in steel molds for the three different geometric shapes (cylinder-CYL, triangular prism-TRP and square prism-SQP) with the same cross-sectional area of 490 mm^2 and length of 80 mm for prisms and 50 mm for cylindrical samples. The samples contain surface skin after foaming.

To adequately compare the mechanical properties of the prepared AAFs under uniaxial compression, it was decided to use the same volume and cross-sectional area of the samples. Standard steel tube with an inner diameter of 25 mm was used as a mold for cylindrical samples (area 491 mm^2). Then, it was necessary to construct and process molds for SQPs and TRPs (see Table 1) so that the inner SQP has a square side of 22.2 mm (area 493 mm^2) and the inner TRP has a side of an equilateral triangle of 33.7 mm (area 495 mm^2).

The AAFs were prepared in designed steel molds in electric resistance furnace at 750 ℃ for 5–6 minutes. Foaming time slightly varied according to the mold shape and length. Prepared AAFs were cut by electric discharge machining to the 30 mm heights. The density (ρ) of the samples was determined from the measured weights and known geometric dimensions of the samples.

From prepared samples (approx. 70 pcs.) three samples of the almost same density for each geometry and alloy was chosen and used for compression tests.

Table 1

Geometry of prepared AAFs for uniaxial compression (height of samples 30 mm)

Shape	Diameter/Side (mm)	Area (mm^2)	Volume (mm^3)
CYL	25.0	491	14726
TRP	33.7	495	14850
SQP	22.2	493	14785

Quasi static uniaxial compression tests were performed at INSTRON testing machine (Instron, Norwood, MA, USA) with the ram speed of 10 mm/min parallel to the remaining outer surface skin on the AAFs with constant density (see Fig. 1). From the obtained stress-strain curves compression strength (CS), plateau stress (σ_{pl}), energy absorption at 50% strain ($EA_{50\%}$) and densification strain (ε_d) were determined according to ISO 13314:2011 [48]. The σ_{pl} was determined as arithmetic mean of stresses at 20% and 40% deformation. The ε_d was determined for stress equal to 130% of σ_{pl}. $EA_{50\%}$ strain was determined by numerical integration of the area under the stress-strain curve until 50% deformation.

Fig. 1 – Different shapes of AAFs for compression tests (AlMg1Si0.6 + 1% wt. ZrH_2, height 30 mm).

Image analysis was performed using ImageJ analysis software to determine the pore area distributions at cut cross sections of investigated AAFs in compression.

3. RESULTS AND DISCUSSION

3. 1. PORE CHARACTERIZATION

Prepared AAF structures are generally heterogeneous (Figs. 2 and 3) at the investigated foam densities. There is basically some heterogeneity trend between top and bottom part of all AAF samples due to foaming in the mold. In addition, significant large pore/heterogeneity could be found at bottom structure of SQP of AlMg1Si0.6 + 1% wt. ZrH_2 foam (pore area 23.966 mm^2) and at bottom structure of SQP (pore area 42.995 mm^2) of AlSi12Mg0.6 + 0.4% wt. TiH_2 foam.

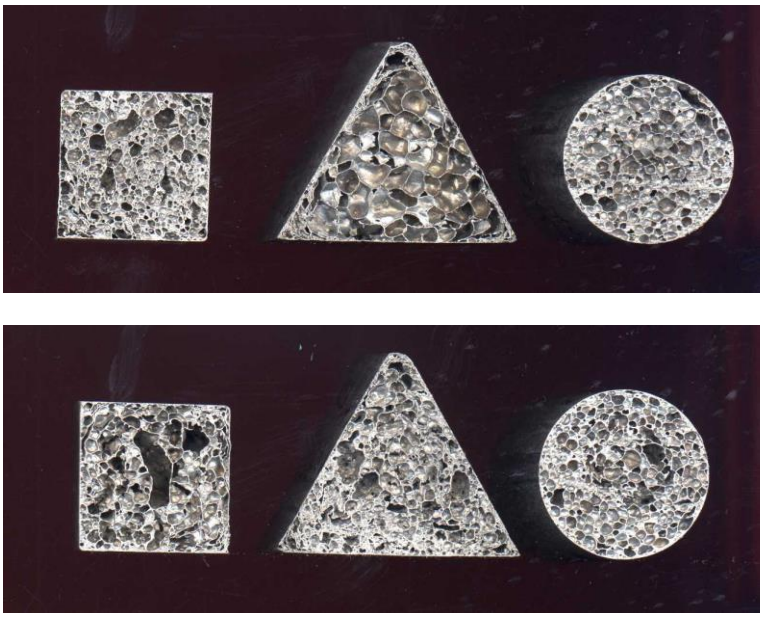

Fig. 2 – Top and bottom structures of AlMg1Si0.6 + 1% wt. ZrH_2 foams (ρ = 0.61 g cm^{-3}).

Computer image analysis (Tables 2 and 3) indicates small differences in number of pores at top and bottom foam structure for all AAFs. Nevertheless, significant difference was observed for number of pores of SQP structures of AlMg1Si0.6 + 1% wt. ZrH_2 foams (208/290) and number of pores of AlSi12Mg0.6 + 0.4% wt. TiH_2 foam cylinder (290/332).

Table 2

Structural analysis of AlMg1Si0.6 + 1% wt. ZrH_2 foams (ρ = 0.61 g cm^{-3})

Shape	N of pores (–)	N of pores top/bottom (–)	Smallest pores < 0.2 mm^2 (%)	Average pores number (–)	Average pores number (%)	Max. pore area (mm^2)
SQP	498	208/290	23	109	22	23.966
TRP	513	265/248	26	126	25	19.090
CYL	766	361/405	28	394	51	8.957

Total number of pores varies according to the cross section shape. It is significantly higher for CYLs in the case of investigated AAFs when compared to TRPs and SQPs at the same composition.

Pore area distributions for almost all samples showed the same dependence for both types of AAFs (Figs. 4–9). The distributions showed bimodal dependence of pore area. The first maximum is as usual for pore areas < 0.20 mm^2. Surprisingly the second maximum is for all shapes and AAF types in the pore area range of 1-5 mm^2. There is only one difference: the second maximum is difficult to distinguish for TRP of AlSi12Mg0.6 + 0.4% wt. TiH_2 foam.

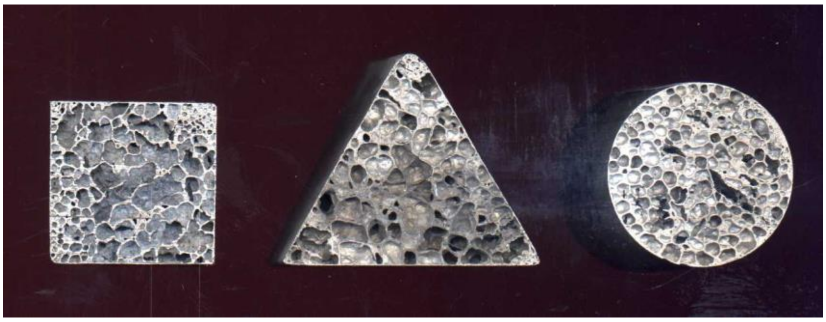

Fig. 3 – Top and bottom structures of tested AlSi12Mg0.6 + 0.4% wt. TiH_2 foams (ρ = 0.71 g cm^{-3}).

Ductile AlMg1Si0.6 + 1% wt. ZrH_2 foam possesses small round pores, the structure is robust with thick pore walls. There is higher number of pores that undergo coalescence/collapse leading to prolonged irregular pores or pores of TRP shape. Thickness of surface skin is almost constant. Some deviation could be observed at the corners of TRP and SQP cross section. The dense areas near edges of TRP and SQP could be considered as thicker surface skin in comparison to cylindrical sample. Maximal pore area is in the range of 8.96 – 23.97 mm^2.

Table 3

Structural analysis of AlSi12Mg0.6 + 0.4% wt. TiH_2 foams (ρ = 0.71 g cm^{-3})

Shape	N of pores (-)	N of pores top/bottom (–)	Smallest pores < 0.2 mm^2 (%)	Average pores number (–)	Average pores number (%)	Max. pore area (mm^2)
SQP	567	284 /283	26	151	27	42.995
TRP	437	221/216	24	96	22	12.526
CYL	622	290 /332	24	163	26	11.635

Brittle AlSi12Mg0.6 + 0.4% wt. TiH_2 foam possess higher number of small pores. Smallest pore areas < 0.2 mm^2 represents 25% of total number of pores, this value is similar to the investigated ductile AAF. The structure is robust with relatively thick pore walls similar to ductile AAF. High number of pores undergo coalescence/collapse leading to prolonged oval/irregular pores. Large fractured pore walls could be observed in bottom part of TRP and SQP structure.

This AAF in general consists of dense and porous regions, that could be simply distinguished. Both regions are the results of coalescence (porous one) and partial collapse (dense one) of pores during late foaming. These structures are the result of used alloy – it is brittle near eutectic aluminum alloy with the high silicon content and small amount of magnesium, i.e., it possesses the higher viscosity of melt and better AAF stability. Together with smaller amount of foaming agent it leads to observed microstructure.

For this reason, the surface skin thickness varies significantly, the dense areas near corners and edges of TRP and SQP could be again considered as thicker surface skin in comparison to cylindrical sample. Maximal pore area is in the range of 11.6 – 43.0 mm^2.

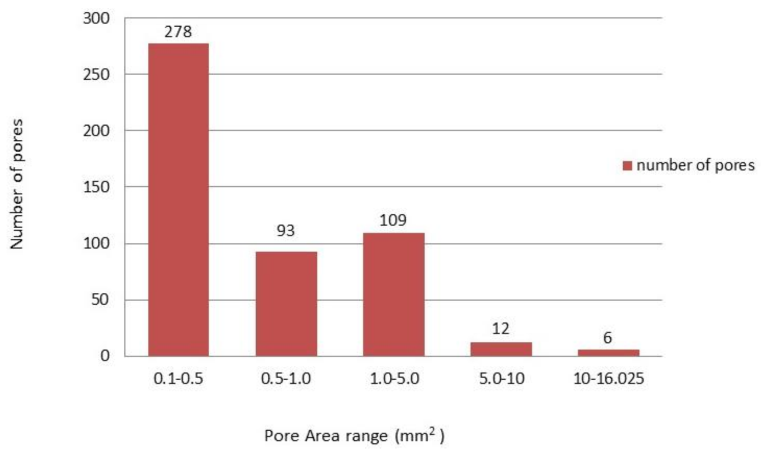

Fig. 4 – Pore area distribution in SQP AlMg1Si0.6 + 1% wt. ZrH_2 foams (0.61 g cm^{-3}).

Cellular structure is a result of dynamic equilibrium between pressure of gas evolved from various foaming agent during heating to melting temperature, during and after melting of aluminum alloy, surface tension between gas and molten aluminum alloy, presence of stabilizing oxides/phases/particles, atmospheric pressure and gravity [3, 27]. AAF cellular structure [1] consists of dense aluminum alloy and empty pores. They are spatially distributed inside the foam volume and this distribution is significantly affected by the technology of AAF preparation. Moreover, closed cell PM foams [3, 15, 19] have always surface skin present on their outer surface.

Approximately constant thickness of surface skin for both types of the used aluminum alloys was observed: Ductile AlMg1Si0.6 + 1% wt. ZrH_2 foam with the density of 0.61 g cm^{-3} and brittle AlSi12Mg0.6 + 0.4% wt. TiH_2 foam with the density of 0.71 g cm^{-3}.

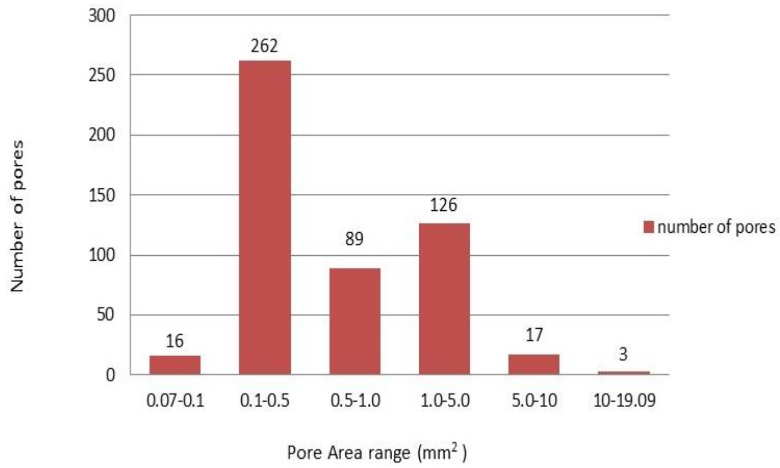

Fig. 5 – Pore area distribution in TRP AlMg1Si0.6 + 1% wt. ZrH_2 foams (0.61 g cm^{-3}).

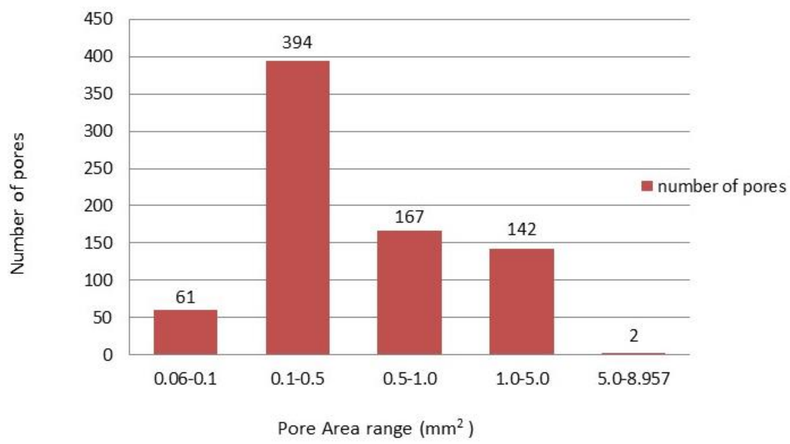

Fig. 6 – Pore area distribution in CYL AlMg1Si0.6 + 1% wt. ZrH_2 foams (0.61 g cm^{-3}).

Coalescence of pores takes place in certain areas thus leading to prolonged oval or irregular pores. This effect could be observed very often near the edges of the mold together with deformed collapsed pores. In comparison to cylindrical sample, the TRP and SQP samples could be considered to have thicker surface skin when the dense areas near edges of them will be counted in.

Summarizing, both AAFs tend to be heterogeneous, with variations between the top and bottom parts due to the foaming process. This agrees with our previous observations for [10] brittle AlSi10 + 1% wt. TiH_2 foams (ρ = 0.69 g cm^{-3}) and ductile AlMg1Si0.6 + 1% wt. TiH_2 foams (ρ = 0.75 g cm^{-3}).

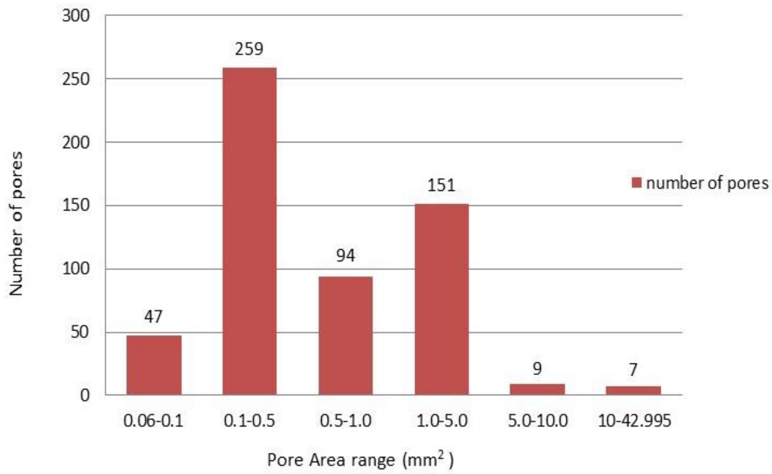

Fig. 7 – Pore area distribution in SQP AlSi12Mg0.6 + 0.4% wt. TiH_2 foams (0.71 g cm^{-3}).

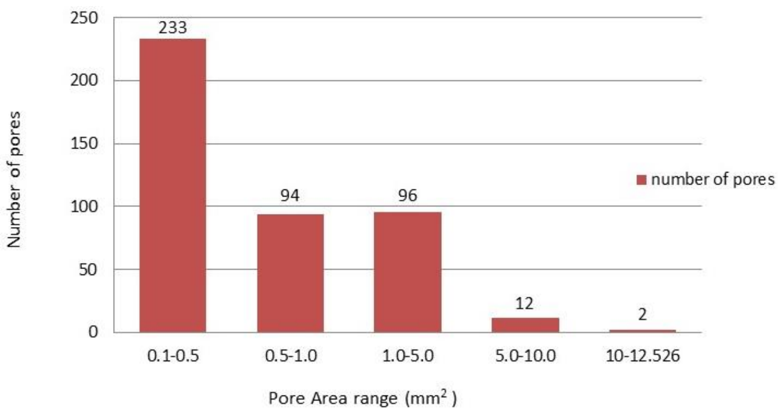

Fig. 8 – Pore area distribution in TRP AlSi12Mg0.6 + 0.4% wt. TiH_2 foams (0.71 g cm^{-3}).

Some shapes of AAFs exhibit significant heterogeneity, especially in the bottom part of certain structures.

Computer image analysis revealed small differences in pore numbers between the top and bottom parts of the AAFs, except for specific cases. The total number of pores varies with cross-sectional shape, being higher for cylindrical AAFs compared to TRP and SQPs of the same composition.

However, investigated ductile AlMg1Si0.6 + 1% wt. ZrH_2 foam (ρ = 0.61 g cm^{-3}) and brittle AlSi12Mg0.6 + 0.4% wt. TiH_2 foam (ρ = 0.71 g cm^{-3}) have significantly smaller number of pores 437–622 and 498–766, respectively in comparison to previously investigated brittle AlSi10 + 1% wt. TiH_2 foams (ρ = 0.69 g cm^{-3}) and ductile AlMg1Si0.6 + 1% wt. TiH_2 foams (ρ = 0.75 g cm^{-3}): 1280–1851 and 890–936, respectively. This could be attributed to different type of foaming agent in the case of ductile AlMg1Si0.6 foams. Slightly different composition together with different amount of TiH_2 inside of AlSi based AAFs 0.4 and 1 wt.% could be the reason in the case of brittle foams.

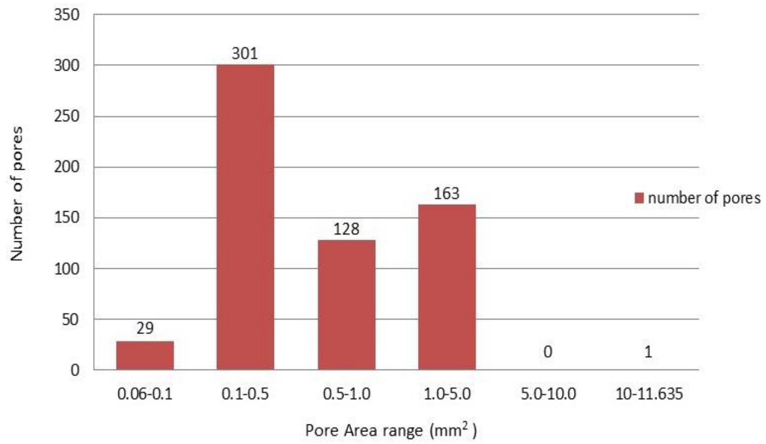

Fig. 9 – Pore area distribution in CYL AlSi12Mg0.6 + 0.4% wt. TiH_2 foams (0.71 g cm^{-3}).

Pore area distributions for both types of AAFs showed a bimodal pattern, with one peak at smaller pore areas and a second peak in the 1–5 mm^2 range. The similar bimodal dependence was observed in previous work [10], however due to higher number of pores the second peak for previously investigated AlSi10 + 1% wt. TiH_2 foams (ρ = 0.69 g cm^{-3}) and ductile AlMg1Si0.6 + 1% wt. TiH_2 foams (ρ = 0.75 g cm^{-3}) was shifted to smaller sizes to the range of 0.1–0.5 mm^2.

From technological point of view, the investigated AAFs possess either smaller amount of foaming agent (0.4 wt.% TiH_2) or foaming agent that fully decomposes at significantly higher temperature (1 wt.%ZrH_2) in comparison with previously investigated AAFs. Therefore, during foaming, there is lower average pressure inside the bubbles in melt, the first bubbles originated from pores or cracks within the precursor material could easily coalescence with smaller pores, thus leading to bimodal structure with second peak at significantly higher pore area.

Ductile AAF samples have round pores, thick pore walls, and show some coalescence or collapse of pores. Surface skin thickness is relatively constant. Brittle AAF samples have more small pores, with thick walls, and distinct dense and porous regions due to coalescence and partial collapse during foaming. Surface skin thickness varies. The situation is the same as for AlSi10 + 1% wt. TiH2 foams (ρ=0.69 g.cm^{-3}) and AlMg1Si0.6 + 1% wt. TiH_2 foams (ρ = 0.75 g cm^{-3}). It can be concluded that ductile AAFs usually tend to have larger and more rounded pores as brittle AAFs and this is the characteristic property of them.

3. 2. COMPRESSION PROPERTIES

AAF samples foamed into the three different shapes (CYL, TRP and SQP) prepared from two different alloys (ductile, brittle) with surface skin possess a characteristic stress-strain curves general for all cellular metals [1]: a linear elastic region up to the first foam layer breakages, plateau region caused by subsequent foam layers' deformation and breaking according to the local porosity variations, and densification of the rests of broken AAF (Figs. 10 and 11). As the ratio of sample height to size/diameter lays within the range of 0.89–1.36, no buckling was observed during compression of AAF samples.

In general, CS of bulk brittle AlSi12Mg0.6 aluminum alloy is around 300 MPa [23]. CS of bulk ductile AlMg1Si0.6 aluminum alloy is around 110 MPa [23], but it can be increased via using of T6 heat treatment up to 120–180% [49]. In this article the compression properties of various shapes of AAFs are compared at the same density. Therefore, this information seems to be redundant, but the reader is requested to keep it in mind when trying to compare AAFs of different composition.

Brittle AlSi12Mg0.6 + 0.4% wt. TiH_2 foam with the density of 0.71 g.cm^{-3} showed significant dependence of compression properties on sample shape: CS and σ_{pl} of TRP and SQPs are significantly smaller (see Table 4). The same situation is for $EA_{50\%}$. The CYL compression properties are the best 23.6 MPa, 23.4 MPa and 11.2 MJm^{-3}, respectively. ε_d is almost similar for all three shapes in the range of 51.1–58.7%. This finding confirms our previous observation [10] that it is independent on the sample shape for AlSi10 + 1% wt. TiH_2 foams and AlMg1Si0.6 + 1% wt. TiH_2 foams.

When we compare the results with previously observed [10] brittle AlSi10 + 1% wt. TiH_2 foam with the density of 0.69 g cm^{-3} it is evident that the microstructure significantly affects probably the shape dependence. For this type of brittle AAF, it was observed that the CS, σ_{pl} and $EA_{50\%}$ were the best for SQP: 20.1 MPa, 27.1 MPa and 12.5 MJ m^{-3}, respectively. In this case the SQP showed significant dense area in AAF core.

It could be noted, that due to the almost similar density and CS of bulk brittle AlSi12Mg0.6 aluminum alloy around 300 MPa, also the investigated compression properties are very similar for AlSi12Mg0.6 and AlSi10 AAFs. Only ε_d has smaller values for AlSi10 foams in the range of 45.8–49.6%. This shift to earlier densification is also probably due to the smaller pores observed in AlSi10 structure in comparison to AlSi12Mg0.6 foam structure.

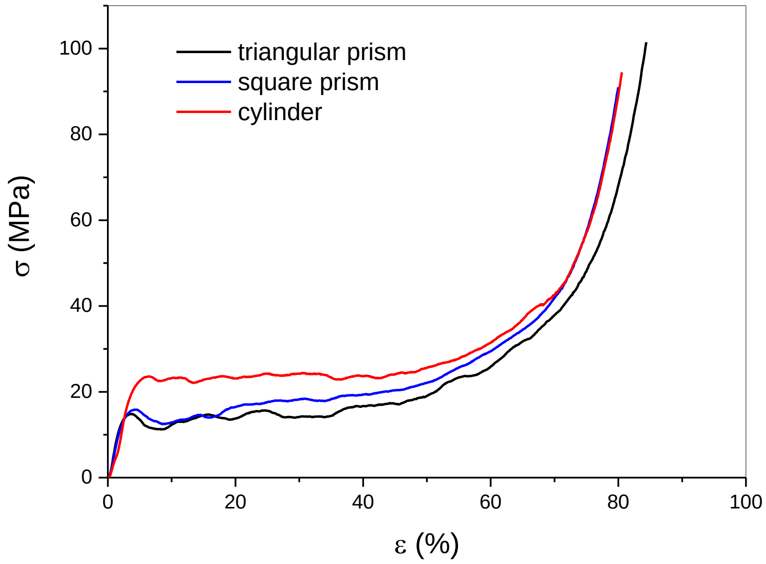

Fig. 10 – Stress-strain curves of AlSi12Mg0.6 + 0.4 % wt. TiH_2 foams (0.71 g cm^{-3}).

If one compares similar brittle AAFs at similar density, it is evident that at the same production technology when alloy and concentration of foaming agent vary, also the final structure varies. When different shapes are foamed from such PM precursors different mechanical properties are obtained in compression. It is still the question of AAF reproducibility and Weibull distribution of mechanical properties [20] for future industrial applications of AAFs in energy absorbers and energy absorbers with PCMs.

Table 4

Compression properties of AlSi12Mg0.6 + 0.4% wt. TiH_2 foams (ρ = 0.71 g cm^{-3})

Shape	CS (MPa)	σ_{pl} (MPa)	$EA_{50\%}$ (MJ m^{-3})	ε_d (%)
TRP	14.9	15.2	7.3	51.1
SQP	15.8	17.9	8.3	52.1
CYL	23.6	23.4	11.2	58.7

Ductile AlMg1Si0.6 + 1% wt. ZrH_2 foam with the density of 0.61 g cm^{-3} showed again significant dependence of compression properties on sample shape: CS and σ_{pl} of TRP are significantly smaller (Table 5). The same situation is for $EA_{50\%}$. The CYL compression properties are the best, but only slightly higher over SQP values: 15.9 MPa, 23.2 MPa and 10.7 MJ m^{-3}, respectively. ε_d in this case is significantly smaller for TRP – 38.5% and around 48.15% for CYL and SQP. ε_d for AlMg1Si0.6 + 1% wt. TiH_2 foam was observed in the range of 41.6–46.7% [10].

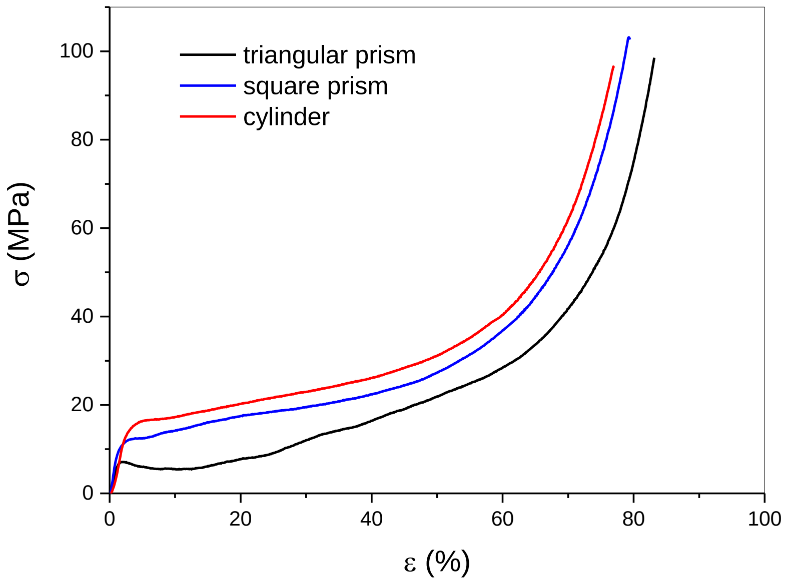

Fig. 11 – Stress-strain curves of AlMg1Si0.6 + 1% wt. ZrH_2 foams (ρ = 0.61 g cm^{-3}).

In previous work [10] ductile AlMg1Si0.6 + 1% wt. TiH_2 foam with the density of 0.75 g.cm^{-3} showed significant dependence of compression properties on sample shape: CS and σ_{pl} of TRP were once again significantly smaller. The same situation was for $EA_{50\%}$. The SQP CS was the best 17.1 MPa. σ_{pl} and $EA_{50\%}$ were the best in this case for CYLs: 31.7 MPa and 14.2 MJ m^{-3}, respectively.

If one compares similar ductile AAFs at different density, it is evident that compression properties of various shapes shows significant density dependence. Higher the density, higher are the compression properties. Only exception is the ε_d.

Table 4

Compression properties of AlMg1Si0.6 + 1% wt. ZrH_2 foams (ρ = 0.61 g cm^{-3})

Shape	CS (MPa)	σ_{pl} (MPa)	$EA_{50\%}$ (MJ m^{-3})	ε_d (%)
TRP	7.1	12.1	5.5	38.5
SQP	12.0	20.0	9.2	48.1
CYL	15.9	23.2	10.7	48.2

Again, at the same production technology and alloy when different type of foaming agent is used, also the final structure varies. When different shapes are foamed from such PM precursors different mechanical properties and response are obtained in compression.

The observed different compression properties of various shapes of AAFs could be predominantly explained by foam structural observations in previous chapter: The thicker surface skin due to inhomogeneous distribution of aluminum and stiffer edges are probably responsible for better performance of SQPs. Nia and Hamedani [50] investigated deformations and EA capacity of thin walled aluminum alloy A3003 tubes with various section shapes (circular, square, rectangular, hexagonal, triangular, pyramidal and conical) both experimentally and numerically. The tubes had the same volume, height, average section area, thickness and material and were subjected under axial quasi static loading. They showed that the section geometry has considerable effect on the EA and force response of tubes. The circular tube had the most EA capacity and the most maximum and the average force of all investigated sections. On the contrary triangular sections absorbed the least amount of energy [51,52], had the smallest maximum and the average force between the tested shapes. This is consistent with our observation for EA and CS of prepared AAFs: $EA_{50\%}$ was the best for cylindrical samples, and this information is very important for EA applications of AAFs [53]. They also confirmed Abramowitz and Wierbicki observation that the larger the number of section edges, the greater the EA capacity [54]. We can conclude that it seems to be correct at least for 3 and 4 edges of AAF tubes.

Summarizing, the inhomogeneity of the structure and variations in surface skin of closed cell AAFs especially in the form of the stiff edges of differently shaped prisms affect CS, σ_{pl} and EA of AAFs significantly. The ε_d is the only one independent property in this case, but decreases with increasing porosity.

4. CONCLUSIONS

The effect of shape on compression behavior of closed cell PM AAFs with surface skin was investigated for CYLs, TRPs and SQPs for ductile AlMg1Si0.6 + 1% wt. ZrH_2 foam with the density of 0.61 g.cm^{-3} and brittle AlSi12Mg0.6 + 0.4% wt. TiH_2 foam with the density of 0.71 g cm^{-3}.

The obtained AAF structures are generally heterogeneous, with certain variations between the top and bottom parts due to the foaming process. Image analysis revealed small differences in the number of pores between the top and bottom AAF parts. The highest difference was for CYLs of brittle AAF (290/332) and SQP of ductile AAF (208/290).

Total number of pores varied according to the cross section shape. It is significantly higher for CYLs when compared to TRPs and SQPs at the same composition. The largest pores were found at the bottom structures of SQP of

AlMg1Si0.6 + 1% wt. ZrH_2 foam (pore area 23.966 mm^2) and of SQP (pore area 42.995 mm^2) of AlSi12Mg0.6 + 0.4% wt. TiH_2 foam.

Ductile AAF possesses small round pores, thick pore walls, and some number of pores that undergo coalescence/collapse, *i.e.*, they are of prolonged irregular or TRP shape. Thickness of surface skin is almost constant, but deviations were observed at the corners of TRP and SQP cross section.

Some of brittle AAFs consist of dense and thin regions. They are the results of coalescence (thin) and partial collapse (dense) of pores during late foaming. These structures are the result of used brittle near eutectic aluminum alloy together with smaller amount of foaming agent.

The investigated AAFs possess either slightly different composition together with smaller amount of foaming agent (0.4 wt.% TiH_2) or foaming agent that fully decomposes at significantly higher temperature (1 wt.%ZrH_2) in comparison with previously investigated AAFs. Therefore, the resulting AAF structure are different as follows: bimodal structure had higher second peak position in the 1–5 mm^2 (previous work range was 0.1–0.5 mm^2). Investigated ductile and brittle AAFs have significantly smaller number of pores 437–622 and 498–766, respectively, in comparison to previously brittle AlSi10 + 1% wt. TiH_2 foams and ductile AlMg1Si0.6 + 1% wt. TiH_2 foams: 1280–1851 and 890–936, respectively.

The compression properties of the AAF samples were confirmed to be shape-dependent. There is only one exception: ε_d was observed independent on the sample shape, type of alloy, type and amount of foaming agent. It is only density dependent.

The SQP sample exhibited the highest CS and σ_{pl} for brittle AlSi12Mg0.6 + 0.4% wt. TiH_2 foam, the $EA_{50\%}$ was the best for CYL. For ductile AlMg1Si0.6 + 1% wt. ZrH_2 foams the cylindrical samples generally outperformed other shapes.

The inhomogeneity in AAF structure, especially in the form of stiff edges in differently shaped prisms, played a crucial role in affecting CS, σ_{pl}, and $EA_{50\%}$ of AAF shapes. It was observed that the technology of preparation is affecting AAF structure and surface skin in such a way that it is affecting compression response of AAF columns of different shape.

Understanding the relationships between AAF structure, surface skin, shape and compression properties is essential for potential industrial applications of these AAFs, such as in energy absorbers, seismic absorbers or heat batteries with PCM.

Acknowledgements. Financial support by Slovak Academy of Sciences and Romanian Academy under the Mobility project contract RA-SAS-22-01. (Project: Applications of metallic foams in intelligent panels and seismic absorbers) is gratefully acknowledged (0.2). Financial support by Slovak government within the project No. 313011BWF3 under the Operational programme Integrated infrastructure (Project: Research on the possibilities of using waste heat from industry for heating in the public and commercial sector in Slovakia) is gratefully acknowledged (0.8).

Received on October 15, 2025

REFERENCES

1. GIBSON, L., ASHBY, M., *Cellular Solids: Structure and Properties*, Cambridge Solid State Science Series, Cambridge University Press, 1997, 2nd ed., doi:10.1017/CBO9781139878326.
2.. ASHBY, M.F., EVANS, A.G., FLECK, N.A., GIBSON, L.J., HUTCHINSON, J.W., WADLEY, H.N.G., *Metal Foams: A Design Guide*, Butterworth-Heinemann, Boston, MA, USA, 2000.
3. BANHART, J., *Manufacture, characterisation and application of cellular metals and metal foams*, Progress in Materials Science, **46**, *6*, pp. 559–632., 2001, doi.org/10.1016/S0079-6425(00)00002-5.
4. DEGISCHER, H.P., KRISZT, B. (Eds.), *Handbook of Cellular Metals*, Wiley-VCH, Weinheim, 2002.
5. SCHWINGE, D., SEELIGER, H.W., VECCHIONACCI, C., ALWES, D., DITTRICH, J., *Aluminium foam sandwich structures for space applications*, Acta Astronautica, **61,** *1–6*, pp. 326–330, 2007, doi.org/10.1016/j.actaastro.2007.01.022.
6. VOILLAT, R., GALLIEN, F., MORTENSEN, A., GASS, V., *Hypervelocity impact testing on stochastic and structured open porosity cast Al-Si cellular structures for space applications*, International Journal of Impact Engineering, **120**, pp. 126–137, 2018, doi.org/10.1016/j.ijimpeng.2018.05.002.
7. EPASTO, G., DISTEFANO, F., GU, L., MOZAFARI, H., LINUL, E., *Design and optimization of Metallic Foam Shell protective device against flying ballast impact damage in railway axles*, Materials & Design, **196**, 109120, 2020, doi:10.1016/j.matdes.2020.109120.
8. GHIANI, C., LINUL, E., PORCU, MC., MARSAVINA, L., MOVAHEDI, N., AYMERICH, F., *Metal Foam-Filled Tubes as Plastic Dissipaters in Earthquake-Resistant Steel Buildings*, IOP Conf. Ser.: Mater. Sci. Eng., **416**, 2018, 012051.
9. GOPINATHAN, A., JERZ, J., KOVACIK, J., *Study of heat transfer characteristics of aluminium foam for PCM-based thermal energy storage applications*, Mechanical Technology and Structural Materials, **70**, pp. 35–42, 2021.
10. KOVACIK, J., JERZ, J., GOPINATHAN, A., SIMANCIK, F., MARSAVINA, L., LINUL, E., *Effect of sample shape on compression behavior of aluminum foams*, Mater. Today Proc., **78**, *2*, pp. 308–313, 2023.
11. MELLER, M.A., *Produit métallique pour l'obtention d'objets laminés, moulés ou autres, et procédés pour sa fabrication*, In French Patent 615.147, 1925.
12. SOSNIK, A., US Patent 2434775, 1948.
13. BJORKSTEN, J., *Ultra-Lightweight Aluminium Foam*, Modern Metals, **13**, *9*, 68–70, 1957.
14. ALLEN, B.C., US Patent 3087 807, 1963.
15. BAUMEISTER, J., *Method for Producing Porous Metal Bodies*, In German Patent 4018360, 29 May 1991.
16. THORNTON, P.H., MAGEE, C.L., *The Deformation of aluminum foams*, Metall Mater Trans A, **6**, pp. 1253–1263, 1975, doi:10.1007/BF02658535.
17. THORNTON, P.H., MAGEE, C.L., *Deformation characteristics of zinc foam*, Metall Mater Trans A, **6**, pp. 1801–1807, 1975, doi:10.1007/BF02642310.
18. BANHART, J., BAUMEISTER, J., *Deformation characteristics of metal foams*, J. Mater. Sci., **33**, pp. 1431–1440, 1998.
19. KOVACIK, J., SIMANCIK, F., *Aluminium foam-modulus of elasticity and electrical conductivity according to percolation theory*, Scripta Materialia, **39**, **2**, pp. 239–246, 1998.
20. SIMANCIK, F., *Reproducibility of aluminium foam properties*, In: *Metal Foam and Porous Metal Structure*, MIT-Verlag, Bremen, 1999, pp. 235–240.
21. KOVACIK, J., SIMANCIK, F., *Comparison of zinc and aluminium foam behaviour*, Kovove Mater, **42**, *2*, pp. 79–90, 2004.
22. KOVACIK, J., MARSAVINA, L., LINUL, E., *Poisson's Ratio of Closed-Cell Aluminium Foams*, Materials, **11**, *10*, 2018, doi:10.3390/ma11101904.

23. KOVACIK, J., JERZ, J., MINARIKOVA, N., MARSAVINA, L., LINUL, E., *Scaling of compression strength in disordered solids: Metallic foams*, Frattura ed Integrita Strutturale, **10**, *36*, pp. 55–62, 2016.
24. LINUL, E., MARSAVINA, L., KOVACIK, J., SADOWSKI, T., *Dynamic and quasi-static compression tests of closed-cell aluminium alloy foams*, Proceedings of the Romanian Academy Series A – Mathematics Physics Technical Sciences Information Science, **18**, *4*, pp. 361–369, 2017.
25. KOVACIK, J., OROVCIK, L., JERZ, J., *High-temperature compression of closed cell aluminium foams*, Kovove Mater, **54**, *6*, pp. 429–440, 2016.
26. GOPINATHAN, A., JERZ, J., KOVACIK, J., DVORAK, T., *Investigation of the relationship between morphology and thermal conductivity of powder metallurgically prepared aluminium foams*, Materials, **14**, 3623, 2021, doi:10.3390/ma14133623.
27. KOVACIK, J., NOSKO, M., MINARIKOVA, N., SIMANCIK, F., JERZ, J., *Closed-Cell Powder Metallurgical Aluminium Foams Reinforced with 3 vol.% SiC and 3 vol.% Graphite*, Processes, **9**, 2031, 2021, doi:10.3390/pr9112031.
28. GOPINATHAN, A., JERZ, J., KOVACIK, J., DVORAK, T., OROVCIK, L., *Study of internal porous structure formation of the powder metallurgically prepared aluminium foam*, J. Phys.: Conf. Ser., **2045**, 012003, 2021.
29. KOVACIK, J., *Correlation between Poisson's ratio and porosity in porous materials*, J. Mater. Sci., **41**, *4*, pp. 1247–1249, 2006, doi.org/10.1007/s10853-005-4237-0.
30. OPIELA, K.C., ZIELINSKI, T.G., DVORAK, T., KUDELA, S.Jr., *Perforated closed-cell aluminium foam for acoustic absorption*, Applied Acoustics, **174**, 107706, 2021, doi.org/10.1016/j.apacoust.2020.107706.
31. GARCIA-MORENO, F., *Commercial applications of metal foams: their properties and production*, Materials, **9**, *2*, 85, 2016, doi:10.3390/ma9020085.
32. SOLORZANO, E., REGLERO, J.A., RODRIGUEZ-PEREZ, M.A.; LEHMHUS, D., WICHMANN, M., de SAJA, J.A., *An experimental study on the thermal conductivity of aluminium foams by using the transient plane source method*, Int. J. Heat Mass Transfer, **51**, *25–26*, pp. 6259–6267, 2008.
33. FIEDLER, T., BELOVA, I.V., ÖCHSNER, A., MURCH, G.E., *Non-linear calculations of transient thermal conduction in composite materials*, Comput. Mater. Sci., **45**, *2*, pp. 434–438, 2009.
34. KORNER, C., *Integral Foam Molding of Light Metals: Technology, Foam Physics and Foam Simulation*, Springer-Verlag, Berlin, Heidelberg, Germany, 2008.
35. CRUPI, V., EPASTO, G., GUGLIELMINO, E., *Comparison of aluminium sandwiches for lightweight ship structures: Honeycomb vs. foam*, Marine Structures, **30**, pp. 74–96, 2013, doi.org/10.1016/j.marstruc.2012.11.002.
36. KHEZRZADEH, O., MIRZAEE, O., EMADODDIN, E., LINUL, E., *Anisotropic compressive behavior of metallic foams under extreme temperature conditions*, Materials, **13**, *10*, 2329, 2020, doi:10.1016/j.ma13102329.
37. ZHANG, Y.R., WANG, G.F., ZHANG, Y.L., YE, J., ZENG, T., ZHAO, K., ZHENG, Z.J., WAN, R., *Crashworthiness design of car threshold based on aluminium foam sandwich structure*, International Journal of Crashworthiness, **27**, *4*, pp. 1167–1178, 2022, doi:10.1080/13588265.2021.1914978.
38. LINUL, E., PIETRAS, D., SADOWSKI, T., MARSAVINA, L., RAJAK, D.K., KOVACIK, J., *Crashworthiness performance of lightweight Composite Metallic Foams at high temperatures*, Composites Part A: Applied Science and Manufacturing, **149**, 106516, 2021, doi.org/10.1016/j.compositesa.2021.106516.
39. UZUN, A., *Compressive crush performance of square tubes filled with spheres of closed-cell aluminum foams*, Archives Of Metallurgy And Materials, **62**, *3*, pp. 1755–1760, 2017.
40. CAROFALO, A., De GIORGI, M., MORABITO, A., *Geometric modelling of metallic foams*, Engineering Computations, **30**, *7*, pp. 924–935, 2013, doi:10.1108/EC-06-2011-0070.

41. BANHART, J., SEELIGER, H.W., *Recent trends in aluminum foam sandwich technology*, Adv. Eng. Mater., **14**, pp. 1082–1087, 2012.
42. LINUL, E., LELL, D., MOVAHEDI, N., CODREAN, C., FIEDLER, T., *Compressive properties of zinc syntactic foams at elevated temperatures*, Composites Part B: Engineering, **167**, pp. 122–134, 2018, doi:10.1016/j.compositesb.2018.12.019.
43. ORBULOV, I.N., SZLANCSIK, A., KEMENY, A., KINCSES, D., *Compressive mechanical properties of low-cost, aluminium matrix syntactic foams*, Composites Part A: Applied Science and Manufacturing, **135**, 105923, 2020, doi:10.1016/j.compositesa.2020.105923.
44. LINUL, E., KHEZRZADEH, O., *Axial crashworthiness performance of foam-based composite structures under extreme temperature conditions*, Composite Structures, **271**, 114156, 2021, doi:10.1016/j.compstruct.2021.114156.
45. MOVAHEDI, N., LINUL, E., *Radial crushing response of ex-situ foam-filled tubes at elevated temperatures*, Composite Structures, **277**, 114634, 2021, doi:10.1016/j.compstruct.2021.114634.
46. RAJAK, D.K., MAHAJAN, N.N., LINUL, E., *Crashworthiness performance and microstructural characteristics of foam-filled thin-walled tubes under diverse strain rate*, Journal of Alloys and Compounds, **775**, pp. 675 – 689, 2019, doi: 10.1016/j.jallcom.2018.10.160.
47. RODINGER, T., ĆORIC, D., ALAR, Ž., *The Influence of Foaming Agents on Aluminium Foam Cell Morphology*, Metals, **13**, 1146, 2023, https://doi.org/10.3390/met13061146.
48. ISO 13314:2011(en), Mechanical testing of metals — Ductility testing — Compression test for porous and cellular metals.
49. OROVCIK, Ľ., NOSKO, M., KOVACIK, J., DVORAK, T., ŠTEPANEK, M., SIMANCIK, F., *Effects of chemical composition on the pore structure and heat treatment on the deformation of PM aluminium foams 6061 and 7075*, Kovove Mater, **54**, *06*, pp. 463–470, 2016.
50. NIA, A.A., HAMEDANI, J.H., *Comparative analysis of energy absorption and deformations of thin-walled tubes with various section geometries*, Thin-Walled Structures, **48**, *12*, pp. 946–954, 2010, doi.org/10.1016/j.tws.2010.07.003.
51. HONG, W., JIN, F., ZHOU, J., XIA, Z., XU, Y., YANG, L., ZHENG, Q., FAN, H., *Quasi-static axial compression of triangular steel tubes*, Thin-Walled Struct., **62**, pp. 10–17, 2013.
52. FAN, Z., LU, G., YU, T., LIU, K., *Axial crushing of triangular tubes*, Int. J. Appl. Mech., **5**, 1350008, 2013.
53. SU, P., HAN, B., WANG, Y., WANG, H., GAO, B., LU, T.J., *Crashworthiness of Foam-Filled Cylindrical Sandwich Shells with Cor-rugated Cores*, Materials, **16**, 6605, 2023, https://doi.org/10.3390/ma16196605.
54. ABRAMOWICZ, W., WIERZBICKI, T., *Axial Crushing of Multicorner Sheet Metal Columns*, ASME. J. Appl. Mech. March, **56**, *1*, pp. 113–120, 1989, doi.org/10.1115/1.3176030.